Acta Crystallographica Section A
Foundations of Crystallography
ISSN 0108-7673

Received 13 July 2012
Accepted 3 January 2013

A tunable multicolour 'rainbow' filter for improved stress and dislocation density field mapping in polycrystals using X-ray Laue microdiffraction

Odile Robach,[a]* Jean-Sébastien Micha,[b] Olivier Ulrich,[a] Olivier Geaymond,[c] Olivier Sicardy,[d] Jürgen Härtwig[e] and François Rieutord[a]

[a]CEA-Grenoble, INAC/SP2M/NRS, 17 rue des Martyrs, 38054 Grenoble Cedex 9, France, [b]UMR SPrAM CNRS-CEA-UJF, CEA-Grenoble, INAC, 17 rue des Martyrs, 38054 Grenoble Cedex 9, France, [c]Institut Néel, CNRS, 25 rue des Martyrs, F-38042 Grenoble, France, [d]CEA-LITEN, MINATEC Campus, 17 rue des Martyrs, 38054 Grenoble Cedex 9, France, and [e]ESRF, 6, rue Jules Horowitz, BP 220, 38043 Grenoble Cedex 9, France. Correspondence e-mail: odile.robach@cea.fr

White-beam X-ray Laue microdiffraction allows fast mapping of crystal orientation and strain fields in polycrystals, with a submicron spatial resolution in two dimensions. In the well crystallized parts of the grains, the analysis of Laue-spot positions provides the local deviatoric strain tensor. The hydrostatic part of the strain tensor may also be obtained, at the cost of a longer measuring time, by measuring the energy profiles of the Laue spots using a variable-energy monochromatic beam. A new 'rainbow' method is presented, which allows measurement of the energy profiles of the Laue spots while remaining in the white-beam mode. It offers mostly the same information as the latter monochromatic method, but with two advantages: (i) the simultaneous measurement of the energy profiles and the Laue pattern; (ii) rapid access to energy profiles of a larger number of spots, for equivalent scans on the angle of the optical element. The method proceeds in the opposite way compared to a monochromator-based method, by simultaneously removing several sharp energy bands from the incident beam, instead of selecting a single one. It uses a diamond single crystal placed upstream of the sample. Each Laue diffraction by diamond lattice planes attenuates the corresponding energy in the incident spectrum. By rotating the crystal, the filtered-out energies can be varied in a controlled manner, allowing one to determine the extinction energies of several Laue spots of the studied sample. The energies filtered out by the diamond crystal are obtained by measuring its Laue pattern with another two-dimensional detector, at each rotation step. This article demonstrates the feasibility of the method and its validation through the measurement of a known lattice parameter.

1. Introduction

Synchrotron radiation X-ray Laue microdiffraction using a white beam has been used for more than a decade (Chung & Ice, 1999; MacDowell *et al.*, 2001; Kunz *et al.*, 2009; Ice & Barabash, 2007; Ice & Pang, 2009; Ulrich *et al.*, 2011; Maass *et al.*, 2006; Ice *et al.*, 2005; Tamura *et al.*, 2000, 2002, 2003; Larson *et al.*, 2002; Kirchlechner *et al.*, 2010, 2011; Hofmann *et al.*, 2009) to determine the strain and orientation fields in polycrystalline materials, with a submicron spatial resolution, in an attempt to elucidate the relations between microstructure and mechanical properties. The existing instruments at the ALS [Advanced Light Source (Berkeley, USA)], APS [Advanced Photon Source (Argonne, USA)] and ESRF [European Synchrotron Radiation Facility (Grenoble, France)] all offer the possibility of switching to a monochromatic beam, to measure, *via* the photon energy, the interplanar distance d_{hkl} of a given (*hkl*) spot.

When the local crystalline quality is sufficient (misorientations/mosaic <1 mrad in the probe volume), the d_{hkl} measurement may be combined with the Laue-pattern measurement to retrieve the complete set of the six lattice parameters and deduce the full elastic strain tensor of the unit cell. This combination requires one to maintain the unit-cell shape and orientation with respect to the incident beam perfectly constant between the two measurements. For the monochromatic method, this implies re-positioning the beam on the inhomogeneous sample with an accuracy better than the typical length inside the sample corresponding to a variation of 10^{-4} on the orientation or the strain. The difficulty

of this alignment led to the development of a white-beam method (Robach *et al.*, 2011) to simultaneously measure the Laue pattern on the two-dimensional detector and the energy of one spot using an energy-resolved point detector mounted sidewards on two translation stages. This method remains slow for raster sample scans as the positioning of the point detector depends on the grain orientation: a prior analysis of the Laue pattern is necessary. This analysis is also necessary for the monochromatic method (unless long energy scans are used to measure several peak energies) to set the monochromator energy close to the approximate spot energy before scanning.

In the case of larger micro-misorientations, the shapes of the Laue spots, and the spot displacements associated with probe volume displacement (orientation gradients), may be analysed to estimate the density of unpaired dislocations [geometrically necessary dislocations (GNDs)]. The energy width of the spots provides the total dislocation density ρ, independently of the paired or unpaired character of the dislocations (Barabash & Ice, 2013) (with a $\rho^{1/2}$ dependence when GNDs are randomly arranged).

This article describes the first tests of another method for measuring the energy position and width of the Laue spots, based on the concept of a rotating 'multicolour filter': instead of using an incident beam with a single energy (as in the monochromatic mode), a white beam is used, in which several well defined energies are missing. A similar method has already been proposed for neutrons (Marmeggi, 1984), except that the rotation was applied to the sample and not to the filter.

2. Experimental details

2.1. Setup and samples

The experiments were performed using the Laue microdiffraction setup of the CRG-IF BM32 beamline at the ESRF (Ulrich *et al.*, 2011). A schematic of the experimental setup is shown in Fig. 1. The standard instrument features microfocusing optics, an *xyz* translation stage for the sample holder inclined by 40° with respect to the white incident beam (energy range 5–22 keV) and a two-dimensional detector (#1) above the sample. Upstream of the focusing optics a multicolour filter system was added which includes the following elements: a vertical gap slit to reduce the beam size down to 0.3 × 0.3 mm, followed by a horizontal translation stage to bring the filter in and out of the beam. This stage carries a vertical translation stage, holding a motorized rotation stage (angle θ_f) with a horizontal axis nearly perpendicular to the incident beam (within 4–5°), itself holding a single-crystalline thin diamond plate (the filter). The diamond plate of 3 × 8 mm, with (110) orientation and 300 µm thickness, makes an angle of approximately 45° with respect to the incident beam. This orientation allows one to have two of the most intense diamond diffraction lines [the (111)'s] in the 9.5–12.5 keV range. A second two-dimensional detector (#2) is placed upstream of the filter near $2\theta = 120°$ to collect the Laue patterns. This allows calculation of the energies of all the beams diffracted by the diamond crystal at any crystal angle, thereby providing the list of energies that will be attenuated in the beam coming to the sample.

The diamond crystal was first mapped (installed in the sample position) by usual Laue microdiffraction, in order to check for the absence of deviatoric strain of the unit cell ($<2 \times 10^{-4}$) and the homogeneity of the unit-cell orientation (better than 0.2 mrad). It was then installed on the rotation stage, on the path of the incident beam. Scans in the filter angle θ_f over 2.5 or 5° with a 0.0025° step were then performed, while recording on detector #1 the Laue patterns of the sample. Two samples were tested in a first campaign: a germanium (111) single-crystal wafer and a polycrystalline bilayer composed of yttria-doped zirconia, forming the electrolyte and anode of a half solid-oxide fuel cell (SOFC). The electrolyte layer in this sample consists of grains of a few microns (Villanova *et al.*, 2010, 2011).

Three other single-crystalline Ge samples (numbered #1, #2, #3) with different orientations were also tested in a second campaign, in order to estimate the uncertainty on the lattice parameter. Table 1 summarizes the geometry of the rotating filter and the sample orientation for the various Ge samples. The orientation of the incident beam with respect to the crystal axes of the filter was chosen to be of low symmetry to be far away from degenerate conditions (when several diamond-diffracted beams have the same energy). This limits the occurrence of very closely spaced dips, which are more difficult to analyse, in the intensity *versus* θ_f curves of the sample's Laue spots.

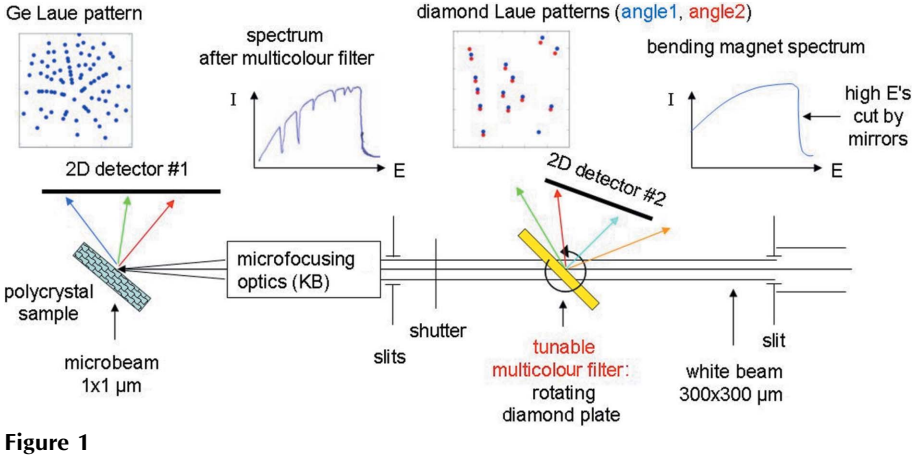

Figure 1
Experimental setup: the multicolour filter setup (vertical gap slit, *x* translation, *z* translation, θ_f rotation, two-dimensional detector #2 at $2\theta = 120°$ in a vertical diffraction plane) is placed about 1 m upstream of the Laue microdiffraction setup (H and V gap slits, Kirkpatrick–Baez mirrors for microfocusing, *xyz* sample translation stage, sample at 40°, two-dimensional detector #1 at $2\theta = 90°$ in a vertical diffraction plane). The filter creates numerous well defined dips in the energy spectrum of the white incident beam. These dips shift in energy with the rotation and successively attenuate the various Laue spots of the sample.

Table 1
Geometry of the rotating filter in the two campaigns and orientation of the Ge samples, as given by the *hkl*s of various characteristic vectors.

$\mathbf{u}_i$ is along the incident beam. **axis** is along the rotation axis. $(\mathbf{z}_1 - \mathbf{y}_1)_{Ge}$ gives the *hkl*s for a (hypothetical) Ge spot at the centre of detector #1. This is used to describe the Ge orientation in rotation around the incident beam. 'dia' and 'Ge' subscripts are used for coordinates with respect to the diamond and Ge lattices, respectively.

Sample	$\mathbf{u}_{i\_Ge}$	$(\mathbf{z}_1 - \mathbf{y}_1)_{Ge}$	$\mathbf{u}_{i\_dia}(\theta_{f0})$	$\mathbf{axis}_{dia}$
0	−0.79 −0.33 −1	0.95 −0.81 1	0.98 0.77 1	0.24 1 −0.92
1	0.09 0.02 1	−0.82 −0.83 −1	−0.92 −0.74 −1	−0.18 −0.96 1
2	0.38 0.18 1	−0.91 0.81 −1	−0.92 −0.74 −1	−0.18 −0.96 1
3	0.65 0.46 1	−1 0.31 −0.57	−0.92 −0.74 −1	−0.18 −0.96 1

The effect of the filter insertion on the X-ray beam size was characterized and found to be negligible for the part of the spectrum above 9.7 keV. Fig. 2 shows the profiles obtained by scanning a rectangular thin film of gold with well defined edges in front of the microbeam and measuring its fluorescence. The slope of the profile stays constant when inserting the filter.

2.2. Data analysis

Each dip observed in the intensity *versus* θ_f curve provides, *via* its position θ_{f_dip}, the energy $E_{exp}(hkl_{sample})$ of the corresponding Laue spot. The experimental value of the lattice spacing a can then be obtained by combining E_{exp} with the local grain orientation and deviatoric strain $(b/a, c/a, \alpha, \beta, \gamma)$ deduced from the Laue pattern. The theoretical value E_{theor} for the spot energy is calculated for a hypothetical lattice parameter a_0, then the $dE/E = (E_{exp}/E_{theor} - 1)$ provides the deviation $-(a - a_0)/a_0$ on the lattice spacing. When using the unstrained lattice parameter as a_0, this directly gives the hydrostatic part of the strain.

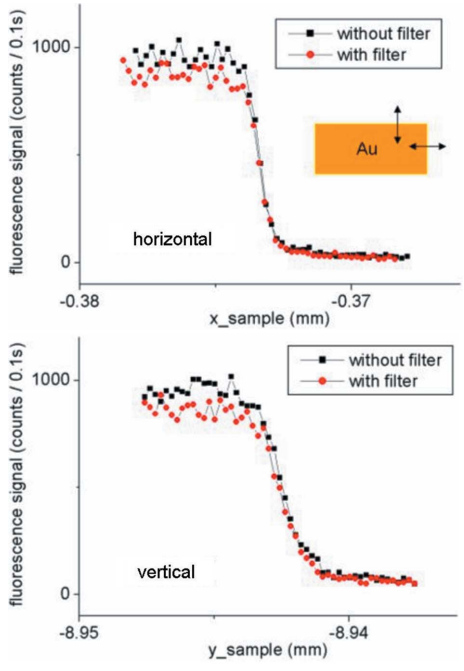

Figure 2
Effect of the insertion of the filter on the size of the X-ray microbeam. Fluorescence profiles on a thin rectangular gold layer on silicon, without (black symbols) and with (red symbols) the filter. The x translation is horizontal and perpendicular to the incident beam. The y translation is at 40° of the incident beam, in the vertical plane containing the beam. Beam size on sample (x, y): (0.8, 1.7) µm.

Alternatively, one set of six lattice parameters (and the full strain tensor) may be obtained by combining the measured energies and Bragg angles of six well chosen Laue spots whose *hkl*s are already known. This may be useful when the accuracy on deviatoric strain provided by the Laue pattern is poor [*e.g.* when Laue spots have a shape incompatible with a precise location (within 0.1 pixel) of their centre of mass].

One important procedure in the analysis is the dip indexing, *i.e.* the assignment of a hkl_{filter} triplet to a given dip observed on a given hkl_{sample} spot. This step is currently done manually using a θ_f *versus* energy graph derived by analysing the Laue patterns of the rotating diamond crystal. In this graph, the experimental dips are reported as points [using $a = a_0$ to calculate the $E_{theor}(hkl_{sample})$ values]. The $E_{filter}(hkl_{filter}, \theta_f)$ curves of the intense *hkl* lines of the diamond are also reported. Fig. 3(*a*) shows for example the graph used to index the dips observed for Ge sample #0. The crossings between the vertical lines $E(hkl_{Ge})$ and the inclined lines $E(hkl_{diamond}, \theta_f)$ provide a list of theoretical dips and also their θ_f positions. Each Laue spot from the sample may therefore undergo several extinctions, if the corresponding vertical line crosses several inclined lines. More than 200 filter lines were expected between 5 and 22 keV, but only 64 are shown here, the ones for which $(f_{polarization} \times f_{atomic})^2$ is larger than 0.1% of the intensity of the most intense line (for which $f_{polarization}$ is nearly 1). The slope of the E_{filter} curves varies with hkl_{filter}, evidencing that different diamond lines provide different energy resolutions for a given angular step. Twenty-five of the diamond lines created detectable dips in this example.

For the Ge samples, the θ_f positions of the dips were analysed to retrieve the Ge lattice parameter. Unit-cell lengths a_0 of 5.6575 and 3.5668 Å were assumed for unstrained Ge and diamond, respectively. The a values were derived by combining E_{dip} measurements with E_{theor} values deduced from the Laue patterns. They will be given as deviations with respect to the theoretical lattice parameter: $dE/E = -da/a = -d\lambda/\lambda$. An important remark is that here the length unit is the diamond lattice parameter. The experimental $(a_{sample} - a_{0\_sample})/a_{0\_sample}$ may therefore contain an unknown $(a_{diamond} - a_{0\_diamond})/a_{0\_diamond}$. One way of checking the diamond lattice parameter would be to use a diamond-diffracted beam whose energy coincides with a fluorescence line of the screen of detector #2.

Based on Bragg's law (*i.e.* neglecting dynamical diffraction effects), the position in θ_f and in $E_{filter} = E_{Ge}$ of an indexed dip can be calculated from 14 scalar parameters, eight of which are fixed: the hkl_{Ge}, the hkl_{filter}, and the diamond and Ge lattice parameters. Six parameters are variable: first the two angles of the incident beam (unit vector $\mathbf{u}_i$) with respect to the Ge unit cell ($\mathbf{u}_{i\_Ge}$) and secondly the geometry of the rotating diamond, which provides the two angles of the incident beam

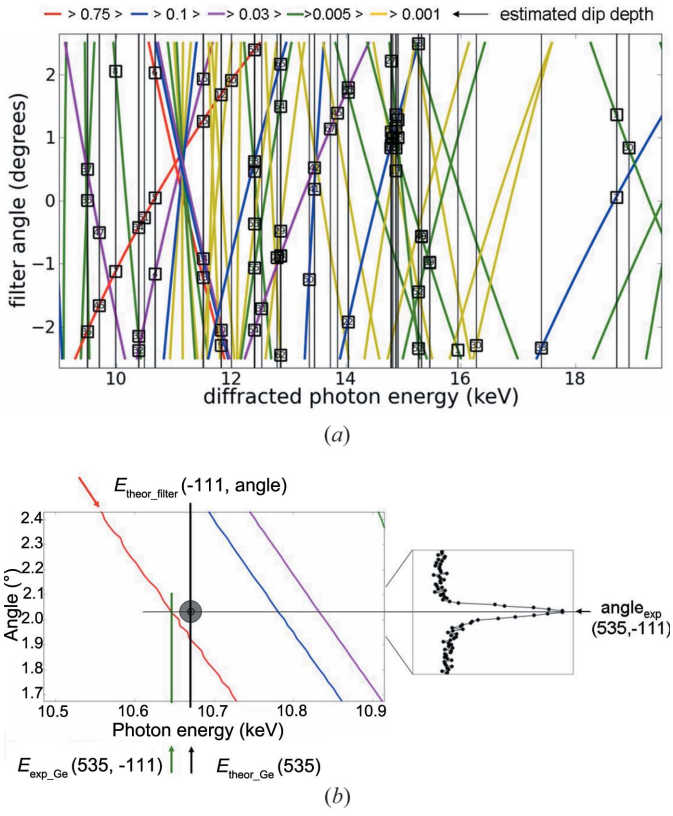

Figure 3
(*a*) Energy *versus* filter angle graph used for indexing the dips in the case of Ge sample #0. The energies of the Ge- and diamond-diffracted beams were calculated from the Laue patterns. The cross points between the $E_{diamond}$ curves and the E_{Ge} vertical lines provide the location of the theoretical dips. The colour code gives a first hint of the dip depth: the theoretical intensity of the diamond-diffracted beams (= 1.0 for the most intense beam). The circles mark the 68 dips experimentally detected on 32 of the Ge spots. Only Ge beams that present dips are shown. Visual comparison between experimental and theoretical dip positions allows one to index the dips. For each Ge-diffracted beam, several vertical lines are needed, as different dips may correspond to different hkl_{Ge} harmonics. (*b*) Interpolation used to convert the experimental θ_{f_dip} position into an experimental energy $E_{exp}(hkl_{sample})$, after having indexed the dip using (*a*).

with respect to the diamond unit cell $[\mathbf{u}_{i\_dia}(\theta_f)]$ for any filter angle θ_f. This geometry is fully described by four parameters: the value of $\mathbf{u}_{i\_dia}$ for a given $\theta_f = \theta_{f0}$, and the two angles of the rotation axis $\mathbf{axis}_{dia}$. Here θ_{f0} is taken at the centre of the scan. To include dynamical diffraction effects, other parameters describing the shape of the diamond (*e.g.* thickness and *hkl*s of the two faces) would need to be added.

When the geometry of the rotating filter is known *via* its four parameters, $\mathbf{u}_{i\_dia}$ can be calculated for any θ_f. Each experimental θ_{f_dip} can then readily be converted into an E_{filter}. Alternatively, a series of $\mathbf{u}_{i\_dia}$ values may be determined by using the refinement of the diamond Laue patterns collected for a series of θ_f values. θ_{f_dip} can then be converted into E_{filter} by interpolating the resulting $E(hkl_{filter}, \theta_f)$ table at $\theta_f = \theta_{f\_dip}$, as shown in Fig. 3(*b*).

In practice, the $E(hkl_{filter}, \theta_f)$ tables provided by the Laue patterns allowed us to correctly index a large number of dips, but led to large deviations between the Ge lattice-spacing values measured using different dips. This was due to a poor accuracy on $\mathbf{u}_{i\_dia}$. For each pattern, eight parameters had been refined using the spot positions: the diamond orientation (three parameters) and the geometry of detector #2 (five parameters).[1] The poor accuracy came from the irregular and elongated shape of the diamond spots on detector #2, which led to large mean pixel deviations (around 1.2 to 1.5) between theory and experiment after refinement. A comparatively much better accuracy was available for $\mathbf{u}_{i\_Ge}$, with mean pixel deviations around 0.1 after refinement of the Ge Laue pattern on detector #1.

It was therefore decided to use the equality of the a_{Ge} values derived from the various Ge dips as a criterion to refine the geometry of the rotating filter, taking advantage of the large number of dips available for Ge (with often several dips per spot). *In fine*, the geometry of the rotating filter was calibrated in two stages. First the diamond Laue patterns collected at the two extreme values of θ_f provided a guess on the geometry. This allowed the indexing of a large fraction of the Ge dips. Then $\mathbf{u}_{i\_dia}(\theta_{f0})$ and $\mathbf{axis}_{dia}$ were refined to minimize the deviation between the a_{Ge} values obtained from different Ge dips.

3. Results

3.1. Germanium single crystals

Fig. 4(*a*) shows the intensity *versus* θ_f profiles for the 32 Laue spots of the Ge single crystal #0 (over a total of 86 spots) that presented one or several measurable extinctions over the scanned 5° range. The Laue patterns of the Ge sample and the diamond filter are shown in Figs. 4(*b*) and 4(*c*). The observed dips in Fig. 4(*a*) varied between 5 and 50%. The angular width of the dips varied between 0.0025 and 0.05° in θ_f, illustrating the dependence of energy resolution on hkl_{filter}. Several dips showed complex shapes, asymmetric or with an 'S' shape. Further work is needed to investigate if dynamical diffraction effects in the thick diamond may explain these shapes. A few expected extinctions (not shown) even led to peaks instead of dips (possibly due to diamond-induced changes in the polarization of the incident beam). A substantial number of extinctions were therefore available (here 68) for sample lattice-parameter measurements.

Table 2 summarizes the results obtained for the Ge lattice parameter for the various samples, after locating the dips in the intensity *versus* θ_f curves (similar to Fig. 4*a*), indexing the dips using a θ_f *versus* energy graph (similar to Fig. 3*a*) and calculating the dE/E for each dip. The number of experimental dips, for a fixed geometry of the rotating filter (and a fixed scanning range), varied from 27 to 60 depending on the sample orientation (for samples #1 to #3). It increased to 68 by (mostly) increasing θ_{f0} by 2° (sample #0).

[1] Here 'geometry of the detector' means the orientation of the incident beam and the three-dimensional position of the unique point in the sample supposedly at the origin of all diffracted rays. All these parameters are referenced to the *Oxyz* frame attached to the detector.

Table 2
Lattice parameter a measured on four Ge single crystals of various orientations.

Values are given as deviations $dE/E = -d\lambda/\lambda = -da/a$ with respect to $a_0 = 5.6575$ Å. Data on sample #0, and on samples #1, #2 and #3, were collected during two different experimental campaigns. The n_{dip} values of dE/E were obtained with a 5° scan in θ_f (step 0.0025°). The refined geometry of the rotating filter is given as deviations with respect to the initial geometry: $dz(\mathbf{u}_i)$ and $dx(\mathbf{u}_i)$ for the incident beam (initially along y), dy(**axis**) and dz(**axis**) for the filter rotation axis (initially close to x). 'opt' indicates the sample used for the refinement of the filter geometry. For the first entry on sample #0, the geometry of the rotating filter was not optimized: the dip energy was obtained by interpolating at $\theta_f = \theta_{f\_dip}$ the $E(hkl_{filter}, \theta_f)$ table provided by the diamond Laue patterns.

	dE/E of Ge dips (10^{-4})					Angular corrections (0.1 mrad) on $\mathbf{u}_{i\_dia}(\theta_{f0})$ and $\mathbf{axis}_{dia}$			
#	Mean	std ±	Range	n_{dip}	opt	dz ($\mathbf{u}_i$)	dx ($\mathbf{u}_i$)	dy (**axis**)	dz (**axis**)
0	−9.8	38	238	68	no	0	0	0	0
0	−0.6	1.0	5.4	68	0	6.0	−13.8	50	−40
1	−0.9	5.0	23.2	60	1	7.4	12.4	300	50
2	1.9	3.9	18.2	37	1	7.4	12.4	300	50
3	−0.7	3.9	20.0	27	1	7.4	12.4	300	50
2	0.7	3.6	17.9	37	2	6.8	11.8	200	20
3	−2.6	3.2	19.8	27	3	6.8	10.8	200	35

When the filter geometry was obtained from the diamond Laue patterns (sample #0, first line), the mean dE/E was large (-9.8×10^{-4}) and the agreement between the dE/E values of the different dips was poor [standard deviation $(dE/E)_{std}$ of $\pm 38 \times 10^{-4}$]. After optimizing $\mathbf{u}_{i\_dia}(\theta_{f0})$ and $\mathbf{axis}_{dia}$ to minimize the $(dE/E)_{std}$ (sample #0, second line), a much better agreement was obtained [$(dE/E)_{std}$ of $\pm 1.0 \times 10^{-4}$], with a low mean dE/E (-0.6×10^{-4}), *i.e.* the measured parameter was in much better agreement with the literature value. This is encouraging, in view of the very simple procedure used for locating the dips (taking the point of minimum intensity in the curve drawn using the most intense pixel of the spot).

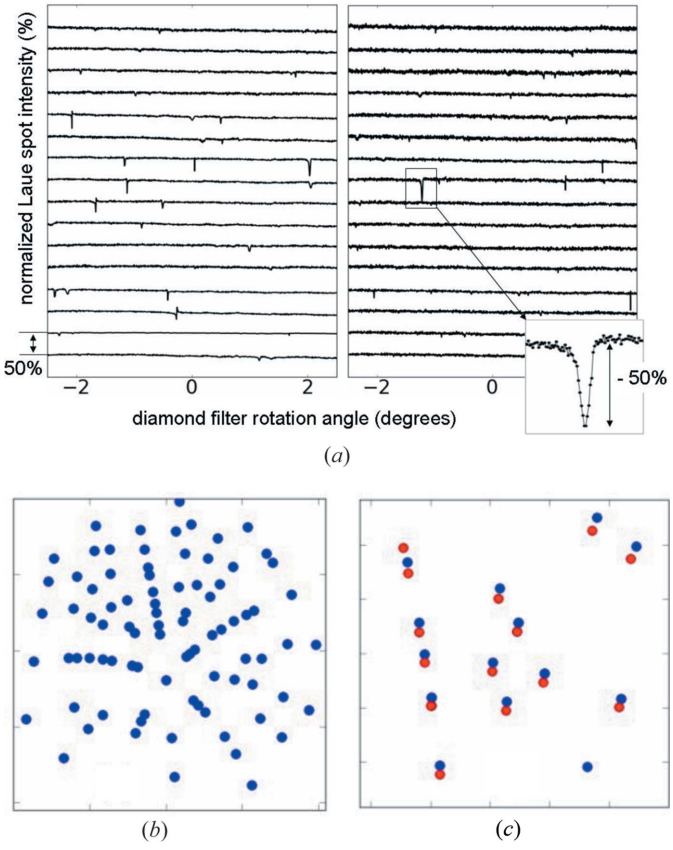

Figure 4
Measurements on the Ge single crystal (sample #0): (*a*) intensity of 32 of the 86 Laue spots *versus* filter angle (5° scan). For each spot, the intensity of a fixed pixel is plotted (the pixel of maximum intensity at $\theta_f = 0$). Intensities are normalized to their values at $\theta_f = -2.5°$. The curves are shifted vertically for clarity. Laue patterns of the Ge sample (*b*) (microbeam, detector #1) and (*c*) the diamond filter [macrobeam, detector #2, $\theta_f = 0$ (blue) and $\theta_f = 0.5°$ (red)].

Minor corrections (below 15 mrad) on the two angles of $\mathbf{u}_{i\_dia}(\theta_{f0})$ were sufficient, while larger corrections were necessary for the two angles of $\mathbf{axis}_{dia}$ (50 to 300 mrad). This reflects the weak sensitivity of $\mathbf{u}_{i\_dia}(\theta_f)$ with respect to the direction of the rotation axis for the small θ_f range used here (±2.5°).

The comparison between samples #1, #2 and #3 allowed an investigation of the accuracy of the refined filter geometry. The geometry was first refined separately on each sample. Then the geometry refined on sample #1 was used to calculate the dE/E's for samples #2 and #3. For the sample-per-sample optimization, the mean dE/E varied between -2.6×10^{-4} and 0.7×10^{-4}. For the optimization on sample #1, it varied between -0.9×10^{-4} and 1.9×10^{-4}. The error on the mean dE/E that comes from the uncertainty on the geometry of the rotating filter is therefore below $\pm 2 \times 10^{-4}$.

Differences in accuracy were noticeable between samples. The final $(dE/E)_{std}$ was three to five times larger for samples #1, #2 and #3 than for sample #0. One possible explanation is a degradation of the energy resolution between the two series of measurements. The microfocusing optics were indeed changed between the two campaigns, to provide a smaller beam size, and the new optics accepted a larger area of the incident beam, leading to twice larger beam divergences on both the sample and the filter. Keeping a low beam divergence may therefore be an issue. The $(dE/E)_{std}$ after refinement also varied with the sample orientation (between 3.2 and 5.0 for samples #1, #2 and #3) for a given filter geometry. These variations may be related to variations in the proportion of sharp dips in the data set.

The analysis performed here is rather crude and the obtained deviation on the dE/E should be perfectible by: (*a*) using a proper description for the shape of the dips, taking into account the dynamical diffraction effects occurring in the thick

diamond crystal; (*b*) using the integrated intensity of the Ge spots instead of the intensity of a single pixel.

The direct determination of the geometry of the rotating filter using the Laue patterns on detector #2 may also become more accurate by using a more realistic hypothesis on the shape of the diamond spots [to describe the elongation due to dynamical diffraction effects (Yan & Noyan, 2005)]. It is not clear yet if it may reach the accuracy already obtained through the criterion of equalizing the dE/E's of all the dips of a Ge single crystal. Another option would be to apply the monochromatic method to the rotating diamond filter to further refine its geometry.

As an element of comparison with the monochromatic method, in terms of number of measured spot energies, the same diamond used as a monochromator set on the ($\bar{1}$11) (see red line on Fig. 3*a*) would provide only ten measurements of the da/a for an equivalent angular scan. With an Si(111) monochromator, a 1000-point angular scan between 10 and 11 keV provided the energy of six Ge spots. The two methods are, however, not fully comparable, as several spot energies are measured more than once with the 'rainbow' method.

3.2. Solid-oxide fuel cell sample with micron-sized grains

The next test consisted of checking the sensitivity of the method for a sample with micron-sized grains. Fig. 5 shows the one-pixel intensity profiles *versus* θ_f (*cf.* Fig. 4*a*) for 32 of the 34 spots showing detectable attenuations for the SOFC sample. These spots were among the 173 most intense (out of around 500) of the multi-grain Laue pattern recorded on a single point of the sample. Photographs of the sample surface and the Laue pattern are also shown. Dip depths up to 60% were observed, indicating that the method should also work here. The analysis of the full local strain tensor for the grains in this sample will be described later. Here a single scan caused extinctions on spots from several grains, providing the da/a for each of them. By comparison, the monochromatic method with large scans (*e.g.* 1 keV) also probes several grains, but without the constant check on beam position provided by the simultaneous Laue-pattern measurement. The white-beam method with the energy-resolved detector probes only one grain for each detector position.

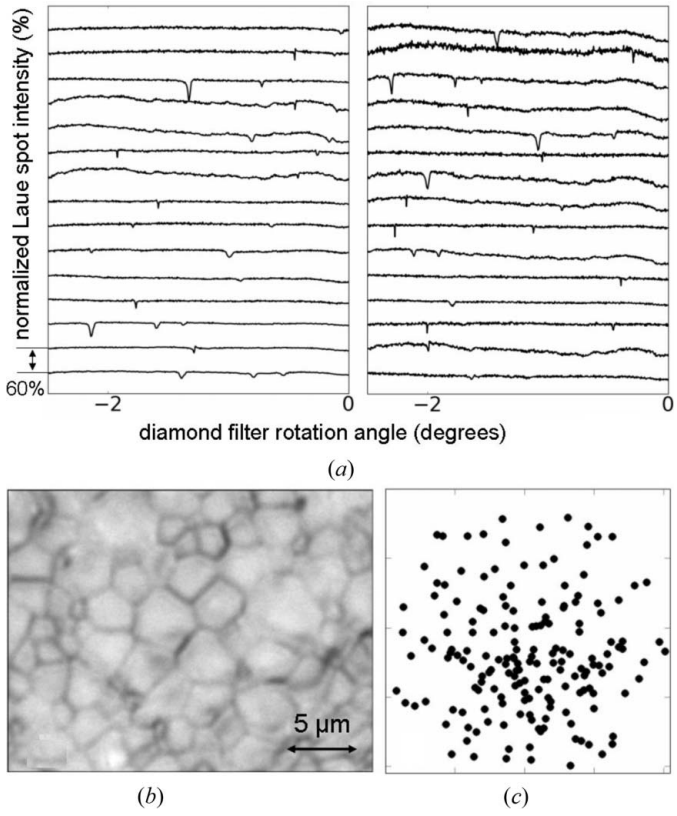

Figure 5
Measurements on a polycrystal with micron-sized grains (electrolyte side of a 'half' solid-oxide fuel cell). The X-ray microbeam is at a fixed position with respect to the sample. (*a*) Intensity of 32 Laue spots from several zirconia grains *versus* filter angle (2.5° scan) (see Fig. 4 for details). (*b*) Optical microscope image (field of view: 30 × 20 µm). (*c*) Multi-grain Laue pattern: positions of the 173 most intense spots.

4. Conclusion and perspectives

The 'rainbow' method provides fast energy profiles for numerous Laue spots, with simultaneous collection of the Laue pattern. The large number of independent measurements of the lattice parameter (68 for a Ge sample with a 5° scan of the filter) should improve the accuracy when trying to measure hydrostatic strain with respect to a known unstrained lattice parameter. A first attempt at measuring the known lattice parameter of an unstrained bulk crystal (Ge) led to a mean da/a of 0.6×10^{-4} (relative error). The $\pm 1.0 \times 10^{-4}$ standard deviation obtained here for a set of 68 measurements is certainly perfectible, by fine tuning of the experimental setup and data analysis.

As a tool to study the full local elastic strain tensor, this method should allow:

(i) Improvement of the reliability of measurements performed by combining the Laue pattern (deviatoric strain) and the energy of one or several spots (absolute value of d_{hkl}).

(ii) Measurement of the full tensor using only spot energies (thanks to the large number of available energy measurements). This may allow one to extend the domain of application of stress measurements to probe volumes with higher orientation gradients.

(iii) Data collection without prior analysis of the Laue pattern (the simultaneously attenuated energies covering a large energy range). For ultimate strain accuracy, online analysis of the Laue pattern will remain useful. This will allow one to adapt the mean θ_f of the scan in order to maximize the number of crossings between intense sample diffraction lines and intense filter-diffracted lines (*cf.* Fig. 3*a*). The usefulness of a second diamond rotation stage for a simultaneous optimization of the number of sharp dips remains to be investigated.

Continuous filter scans with a fast-readout detector (*e.g.* pixel detector) installed near the sample's two-dimensional detector should allow fast mapping of both the Laue pattern and energy profile.

Here the method was tested on lattice-parameter measurements but it also provides the spot-energy width. This should allow fast, simultaneous measurements of dislocation densities for both paired and unpaired dislocations. Short angular scans around a single dip should be sufficient, using the deepest and best-resolved dip [*e.g.* one associated with the $(\bar{1}11)_{\rm filter}$ line]. One application should be the monitoring of the total dislocation density during *in situ* tensile and compressive mechanical tests of single-crystalline micro-pillars (Kirchlechner *et al.*, 2010, 2011; Maass *et al.*, 2006), which require fast measurements without sample motion. This should facilitate the monitoring of the first glide system, which is often difficult to detect *via* spot elongation in the Laue patterns, as it gives few GNDs compared to secondary systems.

We thank the CEA–CNRS staff of the BM32 beamline for technical help with the microdiffraction setup, the ESRF for providing the X-ray beam, P. Gergaud, O. Castelnau, G. Renaud and T. Zhou for participation in the preliminary discussions, H. Isern and P. Montmayeul for technical support, A. Filhol for pointing out the existence of the Marmeggi method, and J. Baruchel for the suggestion to use a fluorescence line of the detector screen for calibration. Financial support was provided by the AMOS ANR-10-NANO-015 project led by J. L. Rouvière. Laue pattern analysis was performed using the *LaueTools* software (LaueTools web site http://sourceforge.net/projects/lauetools/). An alternative name of 'Batterman filter' was proposed by N. Tamura for the method.

References

Barabash, R. I. & Ice, G. E. (2013). *Strain and Dislocation Gradients from Diffraction*, edited by R. I. Barabash & G. E. Ice, ch. 1. London: Imperial College Press/World Scientific Publishing. In the press.

Chung, J. & Ice, G. E. (1999). *J. Appl. Phys.* **86**, 5249–5255.

Hofmann, F., Abbey, B., Song, X., Dolbnya, I. & Korsunsky, A. M. (2009). *Int. J. Mod. Phys. B*, **24**, 279–287.

Ice, G. E. & Barabash, R. I. (2007). *Dislocations in Solids*, edited by F. R. N. Nabarro & J. P. Hirth, ch. 79, pp. 499–601. Amsterdam: Elsevier.

Ice, G. E., Larson, B. C., Yang, W., Budai, J. D., Tischler, J. Z., Pang, J. W. L., Barabash, R. I. & Liu, W. (2005). *J. Synchrotron Rad.* **12**, 155–162.

Ice, G. E. & Pang, J. W. (2009). *Mater. Charact.* **60**, 1191–1201.

Kirchlechner, C., Keckes, J., Micha, J. & Dehm, G. (2011). *Adv. Eng. Mater.* **13**, 837–844.

Kirchlechner, C., Kiener, D., Motz, C., Labat, S., Vaxelaire, N., Perroud, O., Micha, J. S., Ulrich, O., Thomas, O., Dehm, G. & Keckes, J. (2010). *Philos. Mag.* **91**, 1256–1264.

Kunz, M. *et al.* (2009). *Rev. Sci. Instrum.* **80**, 035108.

Larson, B. C., Yang, W., Ice, G. E., Budai, J. D. & Tischler, J. Z. (2002). *Nature (London)*, **415**, 887–890.

Maass, R., Grolimund, D., Petegem, S. V., Willimann, M., Jensen, M., Swygenhoven, H. V., Lehnert, T., Gijs, M. A. M., Volkert, C. A., Lilleodden, E. T. & Schwaiger, R. (2006). *Appl. Phys. Lett.* **89**, 151905.

MacDowell, A. A., Celestre, R. S., Tamura, N., Spolenak, R., Valek, B. C., Brown, W. L., Bravman, J. C., Padmore, H. A., Batterman, B. W. & Patel, J. R. (2001). *Nucl. Instrum. Methods Phys. Res. A*, **467–468**, 936–943.

Marmeggi, J.-C. (1984). *J. Appl. Cryst.* **17**, 286–292.

Robach, O., Micha, J.-S., Ulrich, O. & Gergaud, P. (2011). *J. Appl. Cryst.* **44**, 688–696.

Tamura, N., MacDowell, A. A., Celestre, R. S., Padmore, H. A., Valek, B., Bravman, J. C., Spolenak, R., Brown, W. L., Marieb, T., Fujimoto, H., Batterman, B. W. & Patel, J. R. (2002). *Appl. Phys. Lett.* **80**, 3724–3726.

Tamura, N., MacDowell, A. A., Spolenak, R., Valek, B. C., Bravman, J. C., Brown, W. L., Celestre, R. S., Padmore, H. A., Batterman, B. W. & Patel, J. R. (2003). *J. Synchrotron Rad.* **10**, 137–143.

Tamura, N., Valek, B. C., Spolenak, R., MacDowell, A. A., Celestre, R. S., Padmore, H. A., Brown, W. L., Marieb, T., Bravman, J. C., Batterman, B. W. & Patel, J. R. (2000). *Mater. Res. Soc. Symp. Proc.* **612**, D8.8.3-D8.8.6.

Ulrich, O., Biquard, X., Bleuet, P., Geaymond, O., Gergaud, P., Micha, J. S., Robach, O. & Rieutord, F. (2011). *Rev. Sci. Instrum.* **82**, 033908.

Villanova, J., Sicardy, O., Fortunier, R., Micha, J. & Bleuet, P. (2010). *Nucl. Instrum. Methods Phys. Res. B*, **268**, 282–286.

Villanova, J., Sicardy, O., Fortunier, R., Micha, J. S. & Bleuet, P. (2011). *Mater. Sci. Forum*, **681**, 25–30.

Yan, H. & Noyan, I. C. (2005). *J. Appl. Phys.* **98**, 073527.